Applied Catalysis B: Environmental 197 (2016) 159–167

Contents lists available at ScienceDirect

Applied Catalysis B: Environmental

journal homepage: www.elsevier.com/locate/apcatb

Structure-reactivity relationships in $VO_x/Ce_xZr_{1-x}O_2$ catalysts used for low-temperature NH_3-SCR of NO

Thanh Huyen Vuong, Jörg Radnik, Evgenii Kondratenko, Matthias Schneider, Udo Armbruster, Angelika Brückner*

Leibniz Institute for Catalysis at the University of Rostock, Albert-Einstein-Str. 29a, D-18059 Rostock, Germany

ARTICLE INFO

Article history:
Received 31 December 2015
Received in revised form 24 March 2016
Accepted 27 March 2016
Available online 29 March 2016

Keywords:
Supported V_2O_5 on CeO_2
ZrO_2 and $Ce_xZr_{1-x}O_2$ catalysts
NH_3-SCR of NO
In situ-UV–vis-DRS
In situ-EPR
Pseudo-*in situ*-XPS

ABSTRACT

Supported catalysts with 5 wt.% V_2O_5 on $Ce_xZr_{1-x}O_2$ (x = 1, 0.9, 0.8, 0.7, 0.5, 0.3 and 0) have been prepared and tested in selective catalytic reduction (SCR) of NO by NH_3 between 100 and 300 °C at a GHSV of 70000 h^{-1}. They were also characterized with regard to phase composition, structure of VO_x sites and valence state of vanadium, cerium and zirconium using XRD, ICP-OES, XPS, UV–vis-DRS and EPR, partly *in situ*. $V/Ce_{0.7}Zr_{0.3}O_2$ showed highest activity, N_2 selectivity and stability with almost 100% NO conversion to N_2 at 220 °C and no deactivation during 190 h on stream at 250 °C. Besides high V/(Ce + Zr) surface ratio, fast and reversible VO_x redox cycles revealed to be essential for active catalysts, while Ce and Zr seem to stay tetravalent under reaction conditions. Both, catalytic activity as well as VO_x reduction/reoxidation rates decrease in the order $V/Ce_{0.7}Zr_{0.3}O_2 > V/ZrO_2 > V/CeO_2$. In the best catalyst $V/Ce_{0.7}Zr_{0.3}O_2$, active VO_x sites are effectively connected to the support surface, probably within —O—Ce—O—V(=O)—O—Zr—O— moieties that may support oxygen transport, which is relevant for high SCR activity.

1. Introduction

Since the early 1980s, solid catalysts based on CeO_2 have gained increasing attention for a variety of heterogeneous catalytic redox reactions [1–3]. This is due to the unique ability of CeO_2 to store and release oxygen while non-stoichiometric $[Ce^{4+}_{1-2y}Ce^{3+}_{2y}][O_{2-y}\square_y]$ phases with oxygen vacancies (□) are formed reversibly, in which the Ce valence state can easily shuttle between +4 and +3. This ability is even more pronounced in solid solutions of ceria with isovalent metal cations of smaller diameter such as Zr^{4+} or Ti^{4+} [1]. Due to its high oxidation power, pure ceria is only suitable as catalyst for total oxidations. In contrast, its selectivity can be tuned to a variety of selective heterogeneous catalytic redox reactions by modification with other metal ions [1,2]. One of the most important technical applications is the use of CeO_2-based catalysts in the abatement of exhaust gases. A prominent example is the 3-way catalyst for mobile engines which, however, contains expensive noble metals such as Pt, Pd and Rh as active phase and operates only in a rather high and narrow temperature range of 300–500 °C. On the other hand, selective catalytic reduction (SCR) of nitrogen oxides by ammonia (Eq. (1)) over V_2O_5-WO_3/TiO_2 catalysts is an established technology for cleaning flue gases from power plants in a similar temperature range.

$$4NO + 4NH_3 + O_2 \rightarrow 4N_2 + 6H_2O \quad (1)$$

Taking into account that the temperature of NO_x-containing exhaust gases from other sources such as diesel or lean-burn gasoline engines is much lower, there is a need for the design of catalysts being highly active and selective in low-temperature NH_3-SCR of NO_x—a research field which has seen a lively development in recent years [4]. MnO_x-based catalysts belong to the most active materials for this reaction, enabling total conversion of NO_x already at temperatures as low as 100 °C. However they suffer from rapidly decreasing N_2 selectivity with rising temperature due to undesired N_2O formation and/or from poisoning by other flue gas components such as SO_2 or H_2O [4–6]. Some supported V_2O_5 catalysts showed high NO_x conversion below 250 °C as well, however, depending on the nature of the support, unsatisfactory N_2 selectivity remained a major problem. A few V_2O_5 catalysts, which contain (modified) ceria as support, appeared to be promising for low-temperature NH_3-SCR of NO_x, although they show quite significant differences in their catalytic performance as well [7,8]. This might be due to different structural properties, yet detailed knowledge about their impact on activity and selectivity in NH_3-SCR of NO_x over ceria-supported vanadia catalysts is very limited so far.

* Corresponding author.
E-mail address: angelika.brueckner@catalysis.de (A. Brückner).

http://dx.doi.org/10.1016/j.apcatb.2016.03.063
0926-3373/

Though it can be anticipated that the above mentioned oxygen transport ability of ceria-containing supports might govern the redox activity of the catalysts, it is unclear whether a Ce^{4+}/Ce^{3+} or a V^{5+}/V^{4+} redox cycle or both account for the catalytic activity. Some authors even postulate the participation of significant amounts of V^{3+} [7]. A serious problem and probably a major reason for these discrepancies is that almost all of the conclusions on structure-reactivity relationships in NH_3-SCR of NO_x over ceria-supported VO_x catalysts are based on a comparison of catalytic data with the results of *ex situ* catalyst characterization, which may not reflect the state of the working catalyst. This calls for an in-depth analysis of the redox behavior of supported VO_x/ceria catalysts under relevant reaction conditions.

In this work, we have explored the potential of catalysts containing V_2O_5 dispersed on mixed CeO_2/ZrO_2 supports for the SCR of NO by ammonia at low temperature, since we expected that partial replacement of Ce^{4+} by smaller Zr^{4+} ions promotes defect formation and oxygen transport within the catalyst lattice [9], which in turn could enhance the catalytic performance. Various techniques such as XRD, XPS, EPR, UV–vis diffuse reflectance spectroscopy as well as coupled TPR/UV–vis measurements were used, partly *in situ* under catalytic reaction conditions, to elucidate relations between structural properties and catalytic performance.

2. Experimental

2.1. Catalyst preparation

$Ce_xZr_{1-x}O_2$ supports (x = 1, 0.9, 0.8, 0.7, 0.5, 0.3 and 0) were prepared by a citrate method [10,11]. Appropriate amounts of 0.125 M zirconium nitrate ($ZrO(NO_3)_2{\cdot}6H_2O$, Sigma Aldrich, 99.99%) and 0.125 M cerium nitrate ($Ce(NO_3)_3{\cdot}6H_2O$, Acros, 99,5%) solutions were mixed under vigorous stirring at room temperature to adjust the desired Ce/Zr ratio. A suitable amount of a 10 wt.% citric acid ($C_6H_8O_7{\cdot}H_2O$, Alfa Aesar, 99%) solution was added to this mixed solution to adjust a molar ratio of citric acid/Ce + Zr of 2.5 for the complete complexation of the metal ions. After stirring at room temperature for 1 h, the obtained solution was evaporated at 60–80 °C to form a gel. Subsequently, this viscous gel was dried at 120 °C for 2 h and then calcined in air at 550 °C for 3 h.

The $V/Ce_xZr_{1-x}O_2$ catalysts with a nominal content of 5 wt.% V_2O_5 were prepared by wet impregnation. A certain quantity of ammonium metavanadate (NH_4VO_3, Sigma Aldrich, 99%) was dissolved in 0.2 M oxalic acid ($C_2H_2O_4{\cdot}2H_2O$, Acros, 99.5%) solution. The required amount of the calcined $Ce_xZr_{1-x}O_2$ support powder was suspended in this aqueous solution. After 2 h stirring at room temperature, the excess water was evaporated using a water bath, and the solid residue was oven dried at 120 °C for 12 h and subsequently calcined in air at 400 °C for 5 h [9].

2.2. Catalyst characterization

X-ray diffraction (XRD) powder patterns were recorded at room temperature using a theta/theta diffractometer (X'Pert Pro, Panalytical, Almelo, Netherlands) with Cu Kα radiation (λ = 1.5418 Å. 40 kV, 40 mA) and a X'Celerator RTMS Detector. The data were collected in the 2 Theta range from 5 to 80°. The phase composition of the samples was determined using the program suite WinXPOW by STOE&CIE with inclusion of the Powder Diffraction File PDF2 of the ICDD (International Centre of Diffraction Data). Specific surface areas were determined by nitrogen adsorption at −196 °C using the single-point BET procedure (Gemini III 2375, Micromeritics).

X-ray photoelectron spectra were acquired by a Thermo ESCALAB 220 iXL spectrometer (ThermoFisher Scientific) operating at room temperature with monochromatic Al Kα radiation. The spectra were corrected with respect to the C 1s binding energy value of 284.8 eV. Signal intensities were normalised using the sensitivity factors of Scofield [12] and the transmission function of the spectrometer. For pseudo-*in situ* measurements, catalysts have been pretreated at 200 °C in a reaction chamber attached to the spectrometer under a flow of NH_3-SCR feed (0.4% NH_3, 0.4% NO and 10% O_2/He, total flow rate 25 ml/min) for 30 min, cooled to room temperature and transferred to the analysis chamber without intermediate contact to ambient atmosphere.

EPR spectra were recorded in X-band by a cw-spectrometer ELEXSYS 500-10/12 (Bruker) using a microwave power of 6.3 mW, a modulation frequency and amplitude of 100 kHz and 0.5 mT, respectively. *In situ*-EPR measurements were performed in a home-made quartz plug-flow reactor connected to a gas-dosing device with mass flow controllers (Bronkhorst) at the inlet and a quadrupole mass spectrometer (Omnistar, Pfeiffer Vacuum GmbH) at the outlet for on-line product analysis, under similar conditions as in the catalytic tests at 200 °C [13]. Computer simulation of EPR spectra was performed with the program SIM14S of Lozos et al. [14] using the spin Hamiltonian in Eq. (2).

$$H = \mu_B S g B_o + S A I \quad (2)$$

UV–vis diffuse reflectance spectra were measured using a Cary 5000 spectrometer (Varian) equipped with a diffuse reflectance accessory (praying mantis, Harrick). Baselines were acquired using the bare $Ce_xZr_{1-x}O_2$ supports. For *in situ*-experiments, a heatable reaction chamber (Harrick) equipped with a temperature programmer (Eurotherm) and a gas-dosing system containing mass-flow controllers (Bronkhorst) were used. Kinetic studies of reduction and reoxidation were performed by *in situ*-UV–vis-DRS monitoring of the absorbance at 700 nm in the range of d–d-transitions of reduced V-species [15]. 145 mg of catalyst particles (250–350 μm) were pretreated for 1 h at 275 °C in air and subsequently exposed at 200 °C to a flow of 0.1% NH_3/He and 5% O_2/He (25 ml/min).

Coupled TPR/UV–vis measurements were performed in a quartz tube reactor with 150 mg of catalyst. Before the TPR measurements, the sample was preheated to 400 °C with 8 °C/min in a flow of air, held at this temperature for 30 min and flushed with N_2 for 15 min. Afterwards catalysts were reduced in a flow of 5% H_2/Ar at 400 °C for 1 h. Simultaneous UV–vis-DR spectra were measured using an AVASPEC fiber optical spectrometer (Avantes) equipped with a DH-2000 deuterium-halogen light source and a CCD array detector. A high temperature fiber optical reflection probe was placed inside the reactor furnace perpendicular to the reactor tube [16].

2.3. NH_3-SCR activity test

Catalytic tests were performed in a continuous-flow fixed-bed quartz reactor (length 200 mm, internal diameter 6 mm). The feed contained 1000 ppm NO, 1000 ppm NH_3, 5 vol.% O_2, balance He. For all reactions, 100 mg catalysts of 250–350 μm particle size and the same GHSV of 70000 h^{-1} were used. Analysis of the product mixture was performed by on-line gas chromatography (HP 6890) using a molecular sieve 5A column for analysis of N_2, N_2O and O_2. Simultaneously, the product stream composition was continuously analyzed by a multigas sensor (Limas 11HW, ABB, Germany), including a catalytic converter delivering NO, NO_2, and NH_3 concentrations. Due to inlet temperature and chemical equilibrium, NO was partly converted into NO_2 prior to entering the reactor and this was considered when calculating conversion and selectivity. Reactant and product contents in the effluent gas were monitored during 1 h of continuous reaction in steady state at each temperature chosen. N_2O was formed in negligible amounts (<10 ppm), and hence this product will not be further discussed in this study. A long

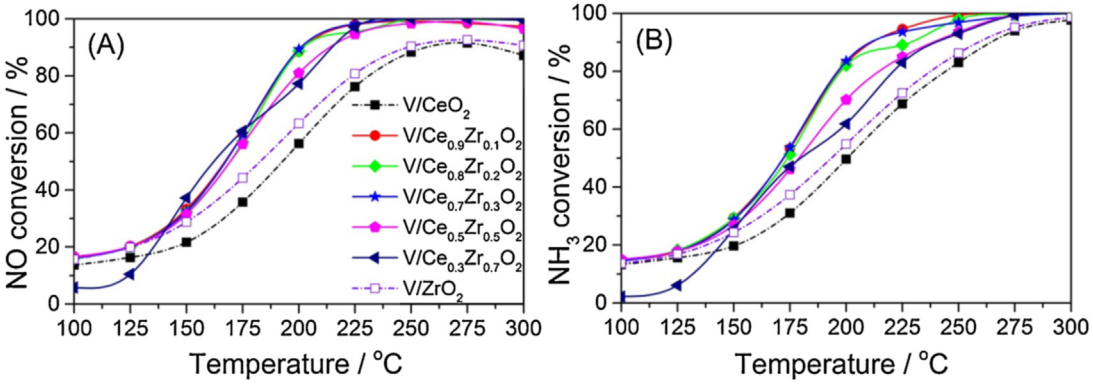

Fig. 1. NO (A) and NH_3 (B) conversion over $V/Ce_xZr_{1-x}O_2$ catalysts as a function of temperature. Feed composition: 0.1% NO, 0.1% NH_3, 5% O_2/He, GHSV = 70000 h^{-1}.

Table 1
Chemical composition, specific surface area and pore volume of supports and catalysts.

Sample	Ce/Zr ratio[a]	V/(Ce + Zr) ratio[a]	V/(Ce + Zr) ratio[b]	Coverage V/nm^2	S_{BET}/m^2 g^{-1}	Pore volume/cm^3 g^{-1}
CeO_2					12.7	0.026
$Ce_{0.9}Zr_{0.1}O_2$					27.3	0.036
$Ce_{0.7}Zr_{0.3}O_2$					49.0	0.038
ZrO_2					25.7	0.032
V/CeO_2		0.100	0.100	27.4	11.5	0.043
$V/Ce_{0.9}Zr_{0.1}O_2$	8.611	0.092	0.097	9.7	31.3	0.046
$V/Ce_{0.7}Zr_{0.3}O_2$	2.356	0.091	0.091	9.8	32.9	0.030
V/ZrO_2		0.071	0.071	12.6	25.0	0.031

[a] Results from ICP.
[b] Theoretical values.

term test of catalyst $V/Ce_{0.7}Zr_{0.3}O_2$ was performed under the same conditions at 250 °C during 190 h.

3. Results and discussion

3.1. Catalytic behavior

Fig. 1 shows the effect of temperature on NO and NH_3 conversion over catalysts with a nominal content of 5% vanadia supported on CeO_2, ZrO_2 and solid $Ce_xZr_{1-x}O_2$ solutions with different Ce/Zr ratio. Catalysts using the same supports with lower and higher V contents were also prepared and tested, yet their activity was lower in all cases. Therefore, these catalysts are not included here.

Despite the fact that V/CeO_2 might contain the highest surface concentration of V (reflected by the highest V/(Ce + Zr) ratio derived from XPS data described below), it is the least active catalyst reaching a maximum NO conversion of 90% at 275 °C which even drops at higher temperature. This might be due to undesired oxidation of NH_3, reflected by $X_{NH3} > X_{NO}$. In comparison to V/CeO_2, V/ZrO_2 is only slightly more active, yet there is negligible decline in NO conversion at high temperature. With the incorporation of small amounts of Zr into CeO_2 the catalytic performance is markedly improved but remains then almost constant upon incorporation of slightly more Zr (compare $Ce_{0.9}Zr_{0.1}O_2$ and $Ce_{0.7}Zr_{0.3}O_2$) and decreases at higher Zr contents. A major problem of V/CeO_2-based catalysts frequently observed is fast deactivation due to the formation of crystalline $CeVO_4$ [8,17]. Therefore, a long-term catalytic test of the best catalyst $V/Ce_{0.7}Zr_{0.3}O_2$ lasting for 190 h has been performed at 250 °C under the same conditions as those in Fig. 1. Fortunately, no decline of the catalytic performance has been observed during this time (Fig. SI-1) indicating that a $CeVO_4$ phase has probably not been formed. This assumption is also supported by Raman measurements of the used $V/Ce_{0.7}Zr_{0.3}O_2$ catalyst in which no characteristic bands for $CeVO_4$ have been detected (Fig. SI-2) [18]. It should also be mentioned that space velocities used in previous tests of V_2O_5/CeO_2-based catalysts in low-temperature NH_3-SCR hardly exceeded 25000 h^{-1} [8]. Thus, performance data obtained here with GHSV = 70000 h^{-1} belong to the best achieved so far.

To gain more information about reasons for the effect of Zr addition to CeO_2 on the SCR activity of $V/Ce_xZr_{1-x}O_2$ catalysts, a comprehensive characterization study has been performed. The following description of results is, however, mainly restricted to the best catalyst $V/Ce_{0.7}Zr_{0.3}O_2$ in comparison to V/CeO_2 and V/ZrO_2.

3.2. Phase composition and surface properties

The XRD powder patterns indicate that the pristine CeO_2 support has a cubic fluorite structure, while pure ZrO_2 comprises a mixture of monoclinic and tetragonal phases (Fig. SI-3). For mixed $Ce_xZr_{1-x}O_2$ oxide supports with x = 0.9 – 0.7, patterns similar to that of CeO_2 have been observed, in which all reflections are gradually shifted to higher 2θ angles with rising Zr content. This indicates a decrease in the lattice constant due to replacement of Ce^{4+} by smaller Zr^{4+} ions and points to the formation of homogeneous solid solutions which maintain the fluorite structure [19,20]. The XRD patterns of the corresponding V-containing catalysts do not show any additional reflections, suggesting the presence of highly dispersed and/or amorphous vanadium oxide species on the surface of the supports. Nevertheless, the Raman spectra show weak bands of V_2O_5 nanocrystallites (too small to be visible by XRD) at 145, 282, 702 and 995 cm^{-1} (Fig. 2) [21]. These bands are most pronounced for V/CeO_2 followed by V/ZrO_2 and weakest for $V/Ce_{0.7}Zr_{0.3}O_2$.

The BET surface area and pore volume of the pure supports increase with the incorporation of Zr in CeO_2 passing a maximum for the composition $Ce_{0.7}Zr_{0.3}O_2$ (Table 1). Deposition of vanadium oxide does not change these values significantly indicating that pore blockage is negligible. The bulk V/(Ce + Zr) atomic ratios are very close to the theoretical value for all catalysts (Table 1).

The electron binding eneries (E_B) of O1s, Zr $3d_{5/2}$ and V $2p_{3/2}$ signals as well as atomic ratios of Ce/Zr and V/(Ce + Zr) determined from XPS are listed in Table 2 and the corresponding spectra are

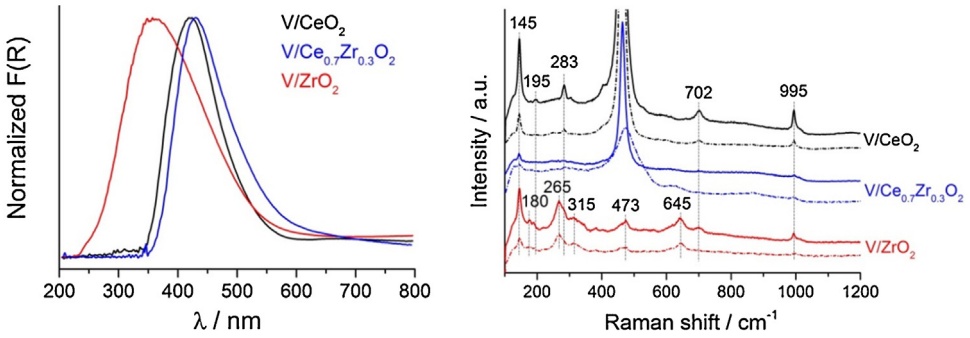

Fig. 2. Left: *In situ*-UV–vis DR spectra of the V/CeO_2, V/ZrO_2, and $V/Ce_{0.7}Zr_{0.3}O_2$ catalysts recorded after 1 h at 275 °C in air and 10 min in He at 200 °C, with CeO_2, ZrO_2, and $Ce_{0.7}Zr_{0.3}O_2$ as baseline; Right: Raman spectra of the same samples before (solid lines) and after 18 h exposure to NH_3-SCR conditions (dashed lines).

Table 2
XPS Binding Energies (eV) and Atomic ratios of fresh and used $V/Ce_xZr_{1-x}O_2$ catalysts.

Sample	Binding energy (eV)			Atomic ratio	
	O1s	Zr $3d_{5/2}$	V $2p_{3/2}$	Ce/Zr	V/(Ce + Zr)
V/CeO_2 fresh		516.5		0.78	
V/CeO_2 used	529.3		516.3		0.70
$V/Ce_{0.9}Zr_{0.1}O_2$ fresh	529.2	184.6	516.4	2.66	0.49
$V/Ce_{0.9}Zr_{0.1}O_2$ used	529.3	183.6	516.7	5.48	0.30
$V/Ce_{0.7}Zr_{0.3}O_2$ fresh	529.7	182.2	516.8	0.68	0.41
$V/Ce_{0.7}Zr_{0.3}O_2$ used	530.8	182.2	516.9	0.94	0.52
V/ZrO_2 fresh	530.2	182.2	517.2		0.30
V/ZrO_2 used	530.2	182.3	517.2		0.31

shown in the supporting information (Figs. SI-4 to SI-6). The O1s E_B value in all fresh and used catalysts is between the values known for pure CeO_2 and ZrO_2, i.e. at 528.6 and 530.6 eV, respectively [22,23]. The Zr $3d_{5/2}$ E_B values in fresh and used V/ZrO_2 and $V/Ce_{0.7}Zr_{0.3}O_2$ catalysts are characteristic for Zr^{4+} species (182–182.4 eV [23,24]), while a shift to higher E_B is observed for the $V/Ce_{0.9}Zr_{0.1}O_2$ catalyst. The lowest amount of substitutional Zr ions in this sample leads to the highest dispersion of Zr in the CeO_2 matrix. This could be the reason for this shift in E_B [22,23]. All samples contain exclusively Ce^{4+} because the peak at 917 eV being typical for Ce^{4+} is present in all samples. Any peaks between 880 and 881 eV typical for Ce^{3+} were not found which exclude the presence of Ce^{3+} [25–28] (see spectra in Fig. SI-6).

For determination of the V valence state, a detailed fitting was not always possible due to the low signal-to-noise ratio and/or the influence of the neighboring O1s peak. Nevertheless, some trends can be deduced from the electron binding energy of the V $2p_{3/2}$ peak which increases with rising ZrO_2 content. For V/CeO_2 E_B values of 516.5 and 516.3 eV being characteristic for V^{4+} are detected [29], while for V/ZrO_2 517.2 eV is found, pointing to V^{5+} [30,31]. The values for V on the mixed supports are in between, pointing to a mixture of tetra- and pentavalent V on these samples. One important result of these *ex situ*-investigations is that only slight differences in the binding energies between the fresh and used samples are detected. To check whether this could be due to possible reoxidation in ambient atmosphere after removing used catalysts from the reactor, pseudo-*in situ*-XPS studies were performed at some selected samples (see below).

In comparison to the bulk V(Ce + Zr) ratios determined by ICP-OES (Table 1), the surface V/(Ce + Zr) ratios derived from XPS measurements of all catalysts are much higher (Table 2), as expected for catalysts prepared by impregnation procedures. However, there exist remarkable differences. The surface V/(Ce + Zr) ratio is highest for V/CeO_2 and decreases with rising Zr content in the support approaching the lowest value for V/ZrO_2. This points to an incorporation of V into the bulk of the support with rising Zr content, probably as V^{4+}, in agreement with previous observations confirming the ability of VO_2 and ZrO_2 to form solid solutions [32–34]. This is suggested, too, by the much higher intensity of the V^{4+} EPR signal of V/ZrO_2 compared to that of the other catalysts, as will be shown below. It is anticipated that V^{4+} can easily replace Zr^{4+} in its lattice positions due to the closer ionic radii, which deviate significantly from that of Ce^{4+} (V^{4+}:72 pm, Zr^{4+}:84 pm, Ce^{4+}:97 pm [35]).

While XPS provides insights into oxidation states and chemical environment of atoms within a few surface layers, EPR and UV–vis diffuse reflectance spectroscopy (DRS) are complementary methods to provide similar information on V^{4+} and V^{5+} species in the whole bulk of samples. UV–vis-DR spectra of the calcined catalysts are governed by charge-transfer (CT) bands of pentavalent V species in a rather wide wavelength range extending up to 550 nm (Fig. 2). Since the bare CeO_2, ZrO_2 and mixed oxide supports absorb light in the UV region below 350 nm as well, the spectra of the catalysts have been recorded using the bare supports as reference white standards. Thus, the features seen in Fig. 2 originate exclusively from vanadium. Frequently, the broad experimental UV–vis spectra of supported vanadia catalysts are deconvoluted into certain superimposed sub-bands to identify different coexisting V_xO_y moieties. Usually, the following band assignments can be found: <300 nm—VO_4 single sites; 300–400 nm—polymerized VO_4 species; 400–420 nm—VO_{4+x} single sites with x = 1 or 2; ≥450 nm—polymerized VO_{4+x} species [31,36–38]. We have not used this deconvolution here, since the spectra of all three catalysts are rather similar and comprise a variety of V_xO_y species ranging from single VO_{4+x} sites to more or less extended V_xO_y clusters. A deconvolution would thus always be a bit arbitrary. However, the spectra in Fig. 2 are all governed by significant absorbance in the range above 400 nm, pointing to the prevalence of more or less polymerized VO_{4+x} species, whereby the extent of polymerization seems to be slightly higher for the binary mixed oxide support compared to the pure oxides. This is also confirmed by the Raman spectra (Fig. 2b), which show besides the main F_{2g} vibration of the fluorite lattice at 463 cm^{-1} [25] small peaks at 145, 195, 283, 702 and 995 cm^{-1} which point to the presence of V_2O_5 nanocrystals, too small to be detected by XRD [21].

In contrast to the Ce containing catalysts, sample V/ZrO_2 shows significant light absorption also below 350 nm which could suggest the presence of VO_4 sites. However, it has to be considered that the absorption edge of the ZrO_2 support may be shifted to higher wavelength upon replacement of Zr^{4+} by distorted $V^{4+}O_{4+x}$ species [32,37], which is suggested by XPS data discussed above in comparison to EPR results described below. Since the pure ZrO_2 support, which shows no bands above 300 nm, was used for recording the base line, this may lead to the observed absorbance below 350 nm in Fig. 2, although it is likely that V ions occupying Zr sites are coor-

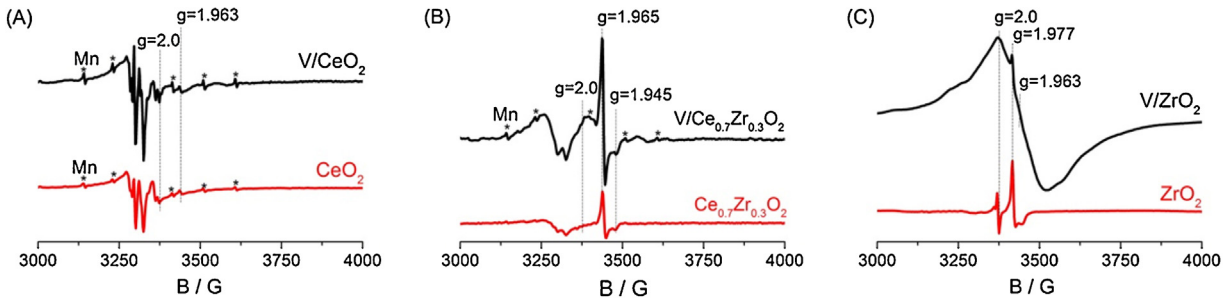

Fig. 3. EPR spectra of CeO_2 and V/CeO_2 (A), $Ce_{0.7}Zr_{0.3}O_2$ and $V/Ce_{0.7}Zr_{0.3}O_2$ (B) and ZrO_2 and V/ZrO_2 (C) recorded at −183 °C.

dinated to more than 4 O ligands since the coordination number of Zr in monoclinic and tetragonal ZrO_2 is 7 or 8, respectively.

EPR spectra of fresh catalysts are shown in Fig. 3 together with the V-free supports. Even in the latter, weak EPR signals are detected, which might arise from paramagnetic oxygen defects such as $O^{\bullet-}$ and/or $O_2^{\bullet-}$ in the range of g = 2.0 and minor Zr^{3+} single sites ($g_\perp = 1.965$, $g_{||} = 1.945$) [39–41].

Occasionally, the latter signals have been assigned to Ce^{3+} [27,42,43], yet this is very unlikely since Ce^{3+} as a $4f^1$ ion is characterized by strong spin-orbit coupling leading to large deviations of the g tensor components from the Landé factor ($g_e = 2.0023$). Thus, tetragonally distorted Ce^{3+} centres with $g_{||} = 3.038$ and $g_\perp = 1.396$ and/or $g_{||} = 0.725$ and $g_\perp = 2.402$ have been detected in crystalline solids with fluorite structure [44,45]. Moreover, due to short relaxation times, Ce^{3+} is detectable usually only at temperatures well below −196 °C. Besides, CeO_2 contains also a Mn^{2+} impurity evidenced by the small hyperfine structure (hfs) sextet (marked with stars in Fig. 3). The EPR spectrum of the as-prepared V/ZrO_2 catalyst contains a broad signal of polymerized VO^{2+} species around g = 1.963 (Fig. 3C). As mentioned above, this may be due to the stabilization of V^{4+} in Zr^{4+} bulk positions, which leads to a depletion of V on the surface as indicated by XPS (compare Tables 1 and 2). Surprisingly, no significant VO^{2+} signal is seen in the EPR spectra of catalysts V/CeO_2 (Fig. 3A) and $V/Ce_{0.7}Zr_{0.3}O_2$ (Fig. 3B), although XPS data suggest that the surface contains some V^{4+} (Table 2). For these two catalysts vanadium is much more enriched on the surface compared to V/ZrO_2. It is probable that the local environment of surface VO^{2+} species differs significantly from those located in deeper layers. This may lead to short relaxation times which would require measurement temperatures below −183 °C to detect those V^{4+} species as it is known, e.g., for tetrahedral V^{4+} [46,47]. On the other hand, it cannot be excluded that some surface V^{5+} is reduced under the UHV conditions of the XPS measurements.

3.3. Behavior of VO_x species in the presence of reactants

Although there is still much debate about the mechanism of the NH_3-SCR over supported vanadia catalysts [48], there seems to be agreement on one important issue, namely the fact that V sites participate in reversible reduction/reoxidation cycles [48–50]. This suggests that the catalyst activity should depend on the redox efficiency of the involved V sites. To analyze this behavior and to find reasons for their different catalytic performance, samples V/CeO_2, V/ZrO_2 and $V/Ce_{0.7}Zr_{0.3}O_2$ have been studied by *in situ*-UV–vis, *in situ*-EPR and pseudo-*in situ*-XPS.

In situ-UV–vis spectra of catalyst $V/Ce_{0.7}Zr_{0.3}O_2$ are shown in Fig. 4A at 200 °C in air and after reaching a steady state in the SCR feed flow after 20 min. Upon switching from air to the SCR feed, the intensity of the CT bands of V^{5+} declines in the region of 400–450 nm while UV–vis absorbance increases above 550 nm in the typical range of d–d transitions of reduced V^{4+}/V^{3+} cations. Interestingly, this V reduction is reversible when NH_3 is removed

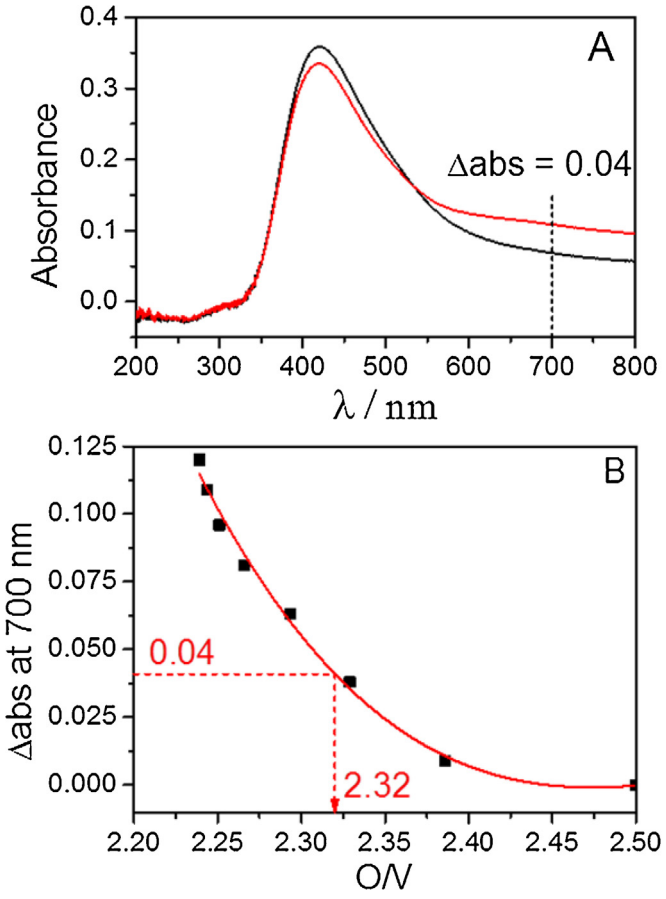

Fig. 4. (A) *In situ*-UV–vis-DR spectra of $V/Ce_{0.7}Zr_{0.3}O_2$ at 200 °C in air (black) and under NH_3-SCR feed flow (red); B) Difference of absorbance at 700 nm as a function of the O/V molar ratio derived from H_2 consumption in a simultaneous TPR/UV–vis experiment. (For interpretation of the references to colour in this figure legend, the reader is referred to the web version of this article.)

from the feed leaving behind only NO/O_2. This indicates that an average V valence state below +5 is established under reaction conditions. A similar behaviour is also observed for V/CeO_2 and V/ZrO_2 (Fig. SI-7). To derive the average V valence state established in the catalysts under SCR conditions, the Δabs (700 nm) values in the *in situ*-UV–vis experiment (Fig. 4A) have been compared with those obtained during a H_2-TPR experiment in which the reactor has been simultaneously coupled to a fiber optical UV–vis spectrometer (Fig. 4B). From the O/V ratio (Fig. 4B, derived from the H_2 consumption) corresponding to the Δabs (700 nm) value in the *in situ*-UV–vis experiment under SCR-conditions (Fig. 4A), average V valences of +4.64, +4.62 and +4.90 are calculated for catalysts $V/Ce_{0.7}Zr_{0.3}O_2$, V/ZrO_2 and V/CeO_2, respectively. Although the mean V valence states under working conditions are almost equal

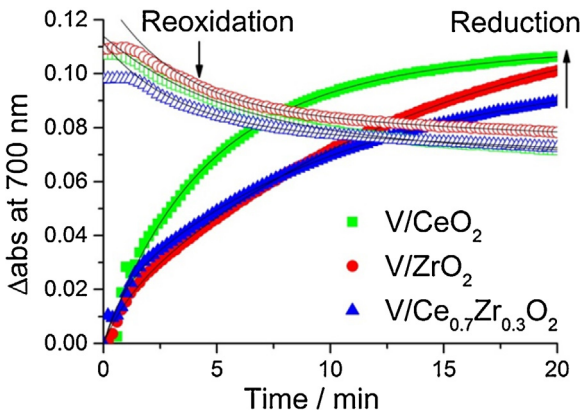

Fig. 5. Difference of absorbance at 700 nm as a function of time for catalysts pretreated at 275 °C in air during reduction in 0.1% NH_3/He and during reoxidation in 5% O_2/He. Experimental data—coloured symbols, black solid lines—kinetic fits using first order rate laws (Eqs. (2) and (3)).

for V/ZrO_2 and $V/Ce_{0.7}Zr_{0.3}O_2$, it must be taken into account that the surface V concentration on ZrO_2 is lower than on $Ce_{0.7}Zr_{0.3}O_2$ (Table 2). This may be one though not the main reason for its lower activity, since the total amount of more active V^{5+}/V^{4+} redox couples is lower in V/ZrO_2. Due to their higher redox potential, the latter species are generally assumed to be more active than V^{4+}/V^{3+} redox couples [15,16,31,51]. However, the rather high mean V valence of +4.90 for V/CeO_2 would hardly fit with this explanation since this catalyst is the least active. This suggests that, apart from the average steady state V valence and the amount of V sites that

Table 3
Rate constants of V reduction and reoxidation (k/min^{-1}, Eqs. (2) and (3)) and mean V valence derived after 20 min under SCR feed flow at 200 °C using simultaneous TPR/UV–vis calibration curves (see Figs. 4, 5 and SI-7).

Sample	V/CeO_2	V/ZrO_2	$V/Ce_{0.7}Zr_{0.3}O_2$
k_{red1}	0.104	0.070	0.095
k_{red2}	0.271	0.960	1.174
k_{reox1}	0.003	0.004	0.005
k_{reox2}	0.181	0.310	0.319
k_{red2}-k_{reox2}	0.090	0.650	0.855
Mean V valence	4.90	4.62	4.64

can undergo reversible redox cycles, the rate of V reduction and reoxidation may be important for the catalytic activity.

Therefore, this property has been analyzed by *in situ*-UV–vis-DRS, too. For this purpose, Δabs (700 nm) in catalysts $V/Ce_{0.7}Zr_{0.3}O_2$, V/ZrO_2 and V/CeO_2 pretreated for 1 h at 275 °C in air flow has been monitored as a function of time after switching to a flow of 0.1% NH_3/He (reduction) and back to a 5% O_2/He flow (reoxidation) (Fig. 5). Experimental data have been fitted using first-order rate laws (Eqs. (2) and (3)), in which C_{red} and C_{reox} denote the concentration of reduced and reoxidized V sites, C^0 values correspond to the respective concentrations of the starting V species and k are the rate constants. Note that concentrations are related to the respective Δabs (700 nm) values, yet absolute concentration values cannot be given, since this would require the knowledge of absorption coefficients. Two different V reduction and reoxidation processes, a fast and a slow one, had to be assumed to obtain satisfactory fits (Table 3).

$$C_{red} = C^0_{ox1}[1\text{-}\exp(-k_{red1}\cdot t)] + C^0_{ox2}[1\text{-}\exp(-k_{red2}\cdot t)] \quad (2)$$

$$C_{reox} = C^0_{red1}[\exp(-k_{reox1}\cdot t)] + C^0_{red2}[\exp(-k_{reox2}\cdot t)] \quad (3)$$

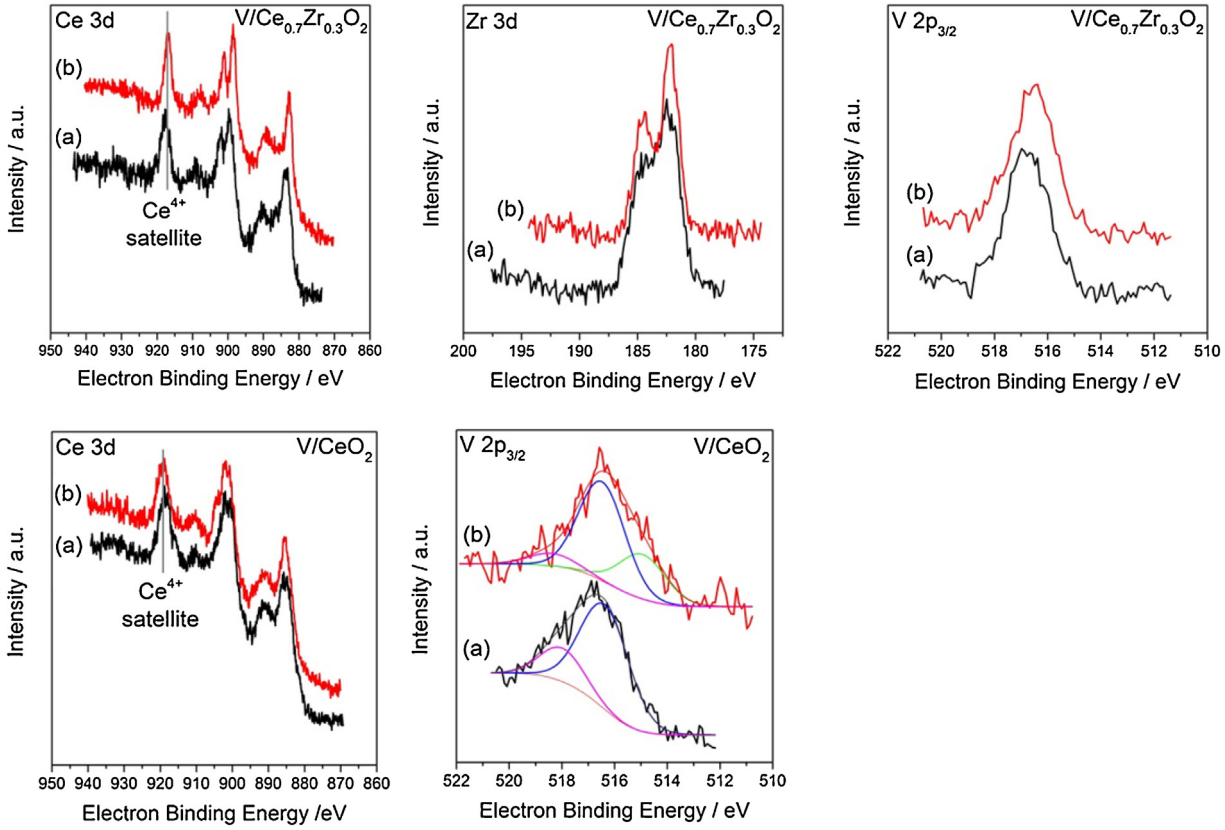

Fig. 6. Pseudo-*in situ*-XP spectra in the region of the Ce 3d, Zr 3d and V $2p_{3/2}$ peaks of catalysts $V/Ce_{0.7}Zr_{0.3}O_2$ (above) and V/CeO_2 (below) measured at room temperature before (a) and after treatment in a flow of 0.4% NO, 0.4% NH_3, 10% O_2/He and transfer to the analysis chamber without contact to ambient atmosphere (b).

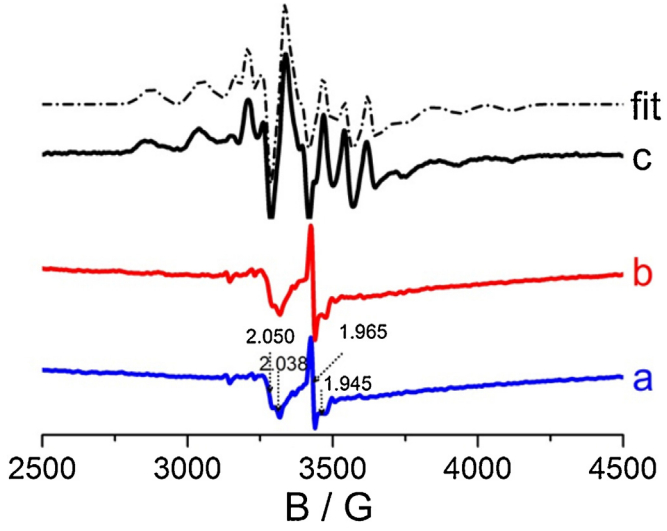

Fig. 7. *In situ* EPR spectra of sample $V/Ce_{0.7}Zr_{0.3}O_2$ recorded at room temperature after (a) 1 h pretreatment in O_2 flow at 400 °C, (b) 30 min exposure to 0.1% NO, 5% O_2/He and (c) 30 min exposure to total SCR feed flow (spectrum b subtracted). The dashed line shows the spectrum fitted with spin Hamiltonian parameters in Table 4.

It is anticipated that the fast processes (reflected by k_{red2} and k_{reox2}) are associated with V sites which are exposed on the outermost surface and readily accessible to reactants while slow processes (reflected by k_{red1} and k_{reox1}) may reflect V sites in deeper layers beneath the surface (Table 3). From Table 3 it is readily evident that for all catalysts reduction is much faster than reoxidation. This might explain why a steady state mean V valence state below +5 is established in all catalysts under SCR conditions. However, while the reduction and reoxidation constants k_1 for the slow subsurface processes are rather similar for all three catalysts, significant differences exist for the constants k_2 reflecting the faster surface processes which might be more relevant for catalysis. The difference in reduction and reoxidation rates k_{red2}-k_{reox2} is almost one order of magnitude smaller for catalyst V/CeO_2 which may account for the high steady state V valence of +4.90. Yet, remarkably, the absolute values of both k_{red2} and k_{reox2} are also the smallest among all three catalysts, which points to slow surface V redox cycles. This may be another reason for low catalytic activity.

Ex situ-XPS data did not provide any evidence for the presence of Ce^{3+} in the catalysts (*vide supra*). To check whether Ce^{3+} may have been formed under reaction conditions but was not detected by *ex situ*-XPS due to subsequent reoxidation in ambient atmosphere, a pseudo-*in situ*-XPS experiment was performed in which catalysts $V/Ce_xZr_{1-x}O_2$ and V/CeO_2 have been pretreated at 200 °C in a flow of NH_3-SCR feed (0.4% NO, 0.4% NH_3, 10% O_2/He) and were then transferred to the analysis chamber without air contact. The Ce^{4+} and Zr^{4+} signals of catalyst $V/Ce_{0.7}Zr_{0.3}O_2$ (Fig. 6) remained unchanged, which clearly indicates that neither Ce^{4+} nor Zr^{4+} is reduced under reaction conditions. After pretreatment in air, the V $2p_{3/2}$ peak is detected at E_B = 516.8 eV being characteristic for a mixture of V^{5+} and V^{4+} as described above. However, a minor shift to E_B = 516.5 eV is observed for this peak after the reaction hinting to the formation of a slightly higher amount of V^{4+}. This agrees pretty well with *in situ*-UV–vis data discussed above in comparison with the presence of a hfs signal of VO^{2+} detected by *in situ*-EPR below (Fig. 7c). The Ce 3d spectrum of sample V/CeO_2 remains, apart from a slight peak narrowing, also almost unchanged, which clearly indicates the presence of only tetravalent Ce.

Interestingly, the V $2p_{3/2}$ spectra of the sample, before and after treatment in the reactant feed, are more complex than that of the mixed oxide. Next to the main peak at 516.6 eV a small shoulder at higher binding energy appeared at the sample before the treatment. This shoulder around 518 eV can be assigned to V^{5+} probably dispersed and strongly interacting with CeO_2. This shoulder almost disappeared after the treatment, but a new shoulder at 515 eV arose instead correlating with trivalent V [29]. This is markedly lower than in catalyst $V/Ce_{0.7}Zr_{0.3}O_2$ and suggests the partial formation of V^{3+} under SCR conditions. This may be another reason for the low activity of catalyst V/CeO_2. In summary, these XPS results suggest that the valence states of Ce and Zr are not affected by the SCR in contrast to V which shows some changes after the reactive treatment.

Table 4
Spin Hamiltonian parameters derived by simulation of difference spectra ($NO/NH_3/O_2$)-(NO/O_2) (Figs. 7 and SI-9).

	$g_\parallel$	$g_\perp$	$A_\parallel$ (G)	$A_\perp$ (G)	$\Delta g_\parallel/\Delta g_\perp$	${\beta^*}_2{}^2$
V/CeO_2	1.922	1.978	182.5	64.0	3.30	0.83
V/ZrO_2	1.922	1.979	189.5	65.5	3.30	0.87
$V/Ce_{0.7}Zr_{0.3}O_2$	A) 1.930	1.970	175.0	59.0	2.24	0.80
	B)[a] 1.924	1.978	185.5	64.0	3.23	0.85

[a] Amounts to ≈20% of all single V^{4+} species.

Additional information about the structure and behavior of V sites in the catalysts has been obtained by *in situ*-EPR spectroscopy. In Fig. 7 EPR spectra are exemplarily shown for the most active catalyst $V/Ce_{0.7}Zr_{0.3}O_2$ (for spectra of the other catalyst see Fig. SI-9). After pretreatment in O_2 and NO/O_2, no V^{4+} species are seen. The signals in spectra a and b originate from species already present in the support and have been discussed above (compare Fig. 3). However, upon switching to the total SCR feed flow, the characteristic hfs signal of VO^{2+} appears (Fig. 7c). Spin Hamiltonian parameters of this signal obtained by simulation of spectrum c are listed in Table 4. To obtain optimum fits, a broad background signal with g_{iso} = 1.963 had to be superimposed in each fit which represents interacting VO^{2+} species but is not listed in Table 4.

It has to be recalled that EPR spectroscopy detects only VO^{2+} species with tetravalent V. However, provided that these species serve as monitors for structural differences of the corresponding VO^{3+} species from which they are formed by reduction, the parameters in Table 4 can be used to derive information on support-dependent structural differences of the V sites in the three catalysts [40,52]. Thus, the parallel component of the hyperfine coupling tensor $A_{||}$ is a measure for the strength of the V=O bond. The higher this value, the shorter is this bond. The ratio $\Delta g_{||}/\Delta g_\perp$ with $\Delta g_{||} = g_{||} - g_e$ and $\Delta g_\perp = g_\perp - g_e$ (g_e = 2.0023) characterizes the total axial distortion. The higher this ratio, the shorter is the V=O bond and the longer are the V—O bonds in the equatorial plane of the VO^{2+} site [52]. The so-called in-plane delocalization coefficient ${\beta^*}_2{}^2$ (Eq. (4), with P = 184.5 G being the strength of the electron-nuclear dipole-dipole interaction for the free V^{4+} ion [53]) reflects the delocalization of the unpaired electron of V^{4+} towards the ligands in the equatorial plane of the VO^{2+} species. It is a measure for the degree of covalence of the V—O bonds. For a purely ionic VO^{2+} species, this coefficient is equal to one. Increasing electron delocalization towards the equatorial O ligands lowers ${\beta^*}_2{}^2$ and reflects rising covalent character of the basal V-ligand bonds [52,54].

$$ {\beta^*}_2{}^2 = (7/6)\Delta g_{||} - (5/12)\Delta g_\perp - (7/6)[(A_{||} - A_\perp)/P] \quad (4) $$

As can be seen from Table 4, the hfs spectrum of catalysts V/ZrO_2 and V/CeO_2 could be fitted with one single VO^{2+} site while two different VO^{2+} species A and B had to be assumed for $V/Ce_{0.7}Zr_{0.3}O_2$. The spin Hamiltonian parameters of the single VO^{2+} sites supported on the pure ZrO_2 and CeO_2 oxides are rather similar to each other and to site B on the mixed oxide. In contrast, VO^{2+} site A on $Ce_{0.7}Zr_{0.3}O_2$ differs significantly in its structure. The smaller $A_{||}$ and $\Delta g_{||}/\Delta g_\perp$ values suggest that this species is less distorted. Its in-

plane delocalization coefficient $\beta^{*}{}_{2}{}^{2}$ is slightly lower compared to values of the other VO^{2+} species which may suggest a slightly more covalent and more effective bonding to the support via V—O—M bridges (M = Zr, Ce). Due to the fact that V sites A are exclusively observed on the mixed oxide support, we tentatively assign them to V sites incorporated in —O—Ce—O—V(=O)—O—Zr—O— surface moieties. Presumably, this attachment is responsible for the fast redox behavior evidenced by UV–vis-DRS (Fig. 5, Table 3).

4. Conclusions

Supported $V/Ce_xZr_{1-x}O_2$ catalysts with x = 0.9 – 0.7 and a vanadia loading of 5 wt.% revealed to be promising catalysts for low-temperature NH_3-SCR of NO, reaching almost 100% of both, NO conversion and N_2 selectivity at 220 °C with essentially no deactivation during at least 190 h and under a space velocity of 70,000 h^{-1}, which is markedly higher than the state of the art [8,55–58]. No undesired formation of N_2O was observed. In contrast, when the pure oxides CeO_2 or ZrO_2 are used as supports instead of the binary $Ce_xZr_{1-x}O_2$ phases, the resulting catalysts were markedly less active. This might be due to significant differences in the nature of the VO_x species which have been shown to participate as active sites in reversible redox cycles under reaction conditions, in which they shuttle between V^{5+} and V^{4+} (detected by *in situ* EPR) while Ce^{4+} and Zr^{4+} do obviously not change their valence states (confirmed by pseudo-*in situ*-XPS). All catalysts are dominated by more or less polymerized VO_{4+x} species, whereby the extent of polymerization seems to be slightly higher on the binary mixed oxide supports and pure CeO_2 compared to pure ZrO_2. In the latter case, significant amounts of VO^{2+} species are incorporated into the bulk of the support, most probably on Zr^{4+} lattice positions, where they might not be accessible by reactants. This is regarded as a major reason for the lower activity of V/ZrO_2 catalysts, which contain less V sites on the surface than catalysts based on pure CeO_2 and $Ce_xZr_{1-x}O_2$. In contrast to V/ZrO_2, the even lower activity of V/CeO_2 is supposed to have other reasons since the surface V/Ce ratio is by a factor of 2 higher than the surface V/Zr ratio. In this catalyst, the rates of reduction and reoxidation of VO_x surface sites are by far the lowest compared to the other catalysts. Since efficient and reversible reduction/reoxidation cycles are essential for catalysts working via a Mars-van Krevelen mechanism (which has been shown to be the case for ceria supported VO_x [59,60]), this may be a major reason for the low activity of V/CeO_2. Moreover, pseudo-*in situ*-XPS data suggest that a significant part of the surface V sites may be reduced to inactive V^{3+} species under SCR conditions. For the most active catalyst $V/Ce_{0.7}Zr_{0.3}O_2$, reduction and reoxidation of surface VO_x sites is fastest. Moreover, EPR data suggest an effective attachment of these VO_x sites to the support surface, probably within —O—Ce—O—V(=O)—O—Zr—O— surface moieties, which themselves may support the redox behavior of the V sites.

Acknowledgements

The authors thank Dr. J. Rabeah, Dr. Jana Engeldinger, Mr. R. Eckelt, and Mrs. A. Simmula for experimental support. Thanh Huyen Vuong acknowledges a grant of the Vietnamese Ministry of Education and Training.

Appendix A. Supplementary data

Supplementary data associated with this article can be found, in the online version, at http://dx.doi.org/10.1016/j.apcatb.2016.03.063.

References

[1] A. Trovarelli, Cat. Rev. 38 (1996) 439–520.
[2] J. Beckers, G. Rothenberg, Green Chem. 12 (2010) 939–948.
[3] L. Vivier, D. Duprez, ChemSusChem 3 (2010) 654–678.
[4] J. Li, H. Chang, L. Ma, J. Hao, R.T. Yang, Catal. Today 175 (2011) 147–156.
[5] J. Zuo, Z. Chen, F. Wang, Y. Yu, L. Wang, X. Li, Ind. Eng. Chem. Res. 53 (2014) 2647–2655.
[6] Z. Liu, Y. Yi, S. Zhang, T. Zhu, J. Zhu, J. Wang, Catal. Today 216 (2013) 76–81.
[7] T. Boningari, R. Koirala, P.G. Smirniotis, Appl. Catal. B 140–141 (2013) 289–298.
[8] C. Li, Q. Li, P. Lu, H. Cui, G. Zeng, Front. Environ. Sci. Eng. 6 (2012) 156–161.
[9] B.M. Reddy, P. Lakshmanan, S. Loridant, Y. Yamada, T. Kobayashi, C. López-Cartes, T.C. Rojas, A. Fernández, J. Phys. Chem. B 110 (2006) 9140–9147.
[10] P.T.M. Pham, M.T. Le, T.T. Nguyen, I.V. Driessche, Materials (2014) 7379–7397.
[11] R.D. Monte, P. Fornasiero, S. Stefano Desinan, J. Kašpar, Chem. Mater. 16 (2004) 4273–4285.
[12] J.H. Scofield, J. Electron. Spectrosc. Relat. Phenom. 8 (1976) 129–137.
[13] R. Pérez Vélez, I. Ellmers, H. Huang, U. Bentrup, V. Schünemann, W. Grünert, A. Brückner, J. Catal. 316 (2014) 103–111.
[14] G.P. Lozos, B.M. Hoffman, C.G. Franz, Quantum Chem. Prog. Exch. (1973), No. 265.
[15] O. Ovsitser, M. Cherian, A. Brueckner, E.V. Kondratenko, J. Catal. 265 (2009) 8–18.
[16] A. Brückner, E. Kondratenko, Catal. Today 113 (2006) 16–24.
[17] W. Daniell, A. Ponchel, S. Kuba, F. Anderle, T. Weingand, D.H. Gregory, H. Knözinger, Top. Catal. 20 (2002) 65–74.
[18] B.M. Reddy, A. Khan, Y. Yamada, T. Kobayashi, S. Loridant, J.-C. Volta, Langmuir 19 (2003) 3025–3030.
[19] C.E. Hori, H. Permana, K.Y.S. Ng, A. Brenner, K. More, K.M. Rahmoeller, D. Belton, Appl. Catal. B: Environ. 16 (1998) 105–117.
[20] B.B.M. Alifanti, N. Blangenois, J. Naud, P. Grange, B. Delmon, Chem. Mater. 15 (2003) 395–403.
[21] X.J. Wang, H.D. Li, Y.J. Fei, X. Wang, Y.Y. Xiong, Y.X. Nie, K.A. Feng, Appl. Surf. Sci. 177 (2001) 8–14.
[22] A. Bensalem, F. Bozon-Verduraz, M. Delamar, G. Bugli, Appl. Catal. A: Gen. 121 (1995) 81–93.
[23] B.M. Reddy, P. Lakshmanan, A. Khan, J. Phys. Chem. B 108 (2004) 16855–16863.
[24] J.F. Moulder, J. Chastain, Handbook of X-ray Photoelectron Spectroscopy: A Reference Book of Standard Spectra for Identification and Interpretation of XPS Data, Physical Electronics Division Perkin-Elmer Corporation, 1992.
[25] B.M. Reddy, P. Bharali, P. Saikia, S.-E. Park, M.W.E. van den Berg, M. Muhler, W. Grunert, J. Phys. Chem. C 112 (2008) 11729–11737.
[26] C. Zhang, J. Lin, Phys. Chem. Chem. Phys. 13 (2011) 3896–3905.
[27] E. Abi-aad, R. Bechara, J. Grimblot, A. Aboukais, Chem. Mater. 5 (1993) 793–797.
[28] E. Bêche, P. Charvin, D. Perarnau, S. Abanades, G. Flamant, Surf. Interface Anal. 40 (2008) 264–267.
[29] M.C. Biesinger, L.W.M. Lau, A.R. Gerson, R.S.C. Smart, Appl. Surf. Sci. 257 (2010) 887–898.
[30] J.F. Moulder, W.F. Stickle, P.E. Sobol, K.D. Bomben, in: J. Chastain, R.C. King Jr. (Eds.), Handbook of X-Ray Photoelectron Spectroscopy, Phys. Electronics Inc., Eden Prairie, USA, 1995, p. 75.
[31] P. Rybarczyk, H. Berndt, J. Radnik, M.M. Pohl, O. Buyevskaya, M. Baerns, A. Brückner, J. Catal. 202 (2001) 45–58.
[32] C. Valentín, J.V. Folgado, J. Alarcoín, Mater. Res. Bull. 36 (2001) 1615–1627.
[33] P. Chandley, R.J.H. Clark, R.J. Angle, G.D. Price, J. Chem. Soc. Dalton Trans. (1992) 1579–1584.
[34] A. Adamski, Z. Sojka, K. Dyrek, M. Che, Solid State Ionics 117 (1999) 113–122.
[35] CRC Handbook of Chemistry and Physics, Internet Version, CRC Press, Boca Raton, FL, 2005, pp. 2092–2094.
[36] H. Berndt, A. Martin, A. Brückner, E. Schreier, D. Müller, H. Kosslick, G.U. Wolf, B. Lücke, J. Catal. 191 (2000) 384–400.
[37] A. Khodakov, B. Olthof, A.T. Bell, E. Iglesia, J. Catal. 181 (1999) 205–216.
[38] A. Brückner, Appl. Catal. A: Gen. 200 (2000) 287–297.
[39] J. Matta, J.-F. Lamonier, E. Abi-Aad, E.A. Zhilinskaya, A. Aboukais, Phys. Chem. Chem. Phys. 1 (1999) 4975–4980.
[40] K. Nowińska, A.B. Więckowski, Z. Phys. Chem. NF 162 (1989) 231–244.
[41] C. Gionco, M.C. Paganini, E. Giamello, R. Burgess, C. Di Valentin, G. Pacchioni, Chem. Mater. 25 (2013) 2243–2253.
[42] P. Ratnasamy, D. Srinivas, C.V.V. Satyanarayana, P. Manikandan, R.S. Senthil Kumaran, M. Sachin, V.N. Shetti, J. Catal. 221 (2004) 455–465.
[43] J.L.G. Fierro, J. Soria, J. Sanz, J.M. Rojo, J. Solid State Chem. 66 (1987) 154–162.
[44] R.W. Schwartz, N.J. Hill, J. Chem. Soc. Faraday Trans. 70 (1974) 124–131.
[45] A. Kiel, W.B. Mims, Phys. Rev. B 6 (1972) 34–39.
[46] V. Havlíček, P. Novák, M. Vichr, Phys. Status Solidi (b) 44 (1971) K21–K24.
[47] D. Ball, B.M. Wanklyn, Phys. Status Solidi (a) 36 (1976) 307–316.
[48] N.Y. Topsøe, Cattech (1997) 125–134.
[49] H. Bosch, F.J.J.G. Janssen, F.M.G. van den Kerkhof, J. Oldenziel, J.G. van Ommen, J.R.H. Ross, Appl. Catal. 25 (1986) 239–248.
[50] K. Jug, T. Homann, T. Bredow, J. Phys. Chem. A 108 (2004) 2966–2971.
[51] B.M. Weckhuysen, D.E. Keller, Catal. Today 78 (2003) 25–46.
[52] T. Risse, D. Hollmann, A. Bruckner, Catal.: R. Soc. Chem. 27 (2015) 1–32.
[53] B.R. McGarvey, J. Phys. Chem. 71 (1967) 51–66.

[54] L.J. Boucher, E.C. Tynan, T.F. Yen, Electron Spin Resonance of Metal Complexes, Plenum Press, New York, 1969, pp. 111–130.
[55] K.J. Lee, P.A. Kumar, M.S. Maqbool, K.N. Rao, K.H. Song, H.P. Ha, Appl. Catal. B: Environ. 142–143 (2013) 705–717.
[56] W. Zhao, Q. Zhong, Y. Pan, R. Zhang, Chem. Eng. J. 228 (2013) 815–823.
[57] H.H. Phil, M.P. Reddy, P.A. Kumar, L.K. Ju, J.S. Hyo, Appl. Catal. B: Environ. 78 (2008) 301–308.
[58] J. Wang, Z. Yan, L. Liu, Y. Chen, Z. Zhang, X. Wang, Appl. Surf. Sci. 313 (2014) 660–669.
[59] C. Popa, M.V. Ganduglia-Pirovano, J. Sauer, J. Phys. Chem. C 115 (2011) 7399–7410.
[60] B. Beck, M. Harth, N.G. Hamilton, C. Carrero, J.J. Uhlrich, A. Trunschke, S. Shaikhutdinov, H. Schubert, H.-J. Freund, R. Schlögl, J. Sauer, R. Schomäcker, J. Catal. 296 (2012) 120–131.